Journal of Volcanology and Geothermal Research 427 (2022) 107554

Contents lists available at ScienceDirect

Journal of Volcanology and Geothermal Research

journal homepage: www.journals.elsevier.com/journal-of-volcanology-and-geothermal-research

Subsidence of the lava flows emitted during the 2012–2013 eruption of Tolbachik (Kamchatka, Russia): Satellite data and thermal model

M.S. Volkova [a,*], N.M. Shapiro [a,b], O.E. Melnik [c], V.O. Mikhailov [a,d], P.Yu. Plechov [e], E.P. Timoshkina [a], O.V. Bergal-Kuvikas [f,a]

[a] Schmidt Institute of Physics of the Earth, RAS, 10 B. Gruzinskaya St., Moscow 123995, Russian Federation
[b] Institut des Sciences de la Terre, Université Grenoble Alpes, CNRS (UMR5275), 1381, rue de la Piscine, 38610 Gieres, France
[c] Institute of Mechanics, Lomonosov Moscow State University, Russian Federation
[d] Lomonosov Moscow State University, Department of Physics, Russian Federation
[e] Fersman Mineralogical Museum RAS, Bldg. 2, 18 Leninsky Prospekt, Moscow, Russian Federation
[f] Institute of Volcanology and Seismology FEB RAS, 9 Piipa Blvd., Petropavlovsk-Kamchatsky 683006, Russian Federation

ARTICLE INFO

Keywords:
2012–2013 Tolbachik fissure eruption
Lava flow
Lava cooling
Subsidence
InSAR
Thermal model

ABSTRACT

We estimated the subsidence rate of the lava flow formed during the 2012–2013 eruption of Tolbachik volcano from satellite radar interferometry with using Sentinel-1 satellite images between 2017 and 2019. The maximum subsidence values were 285 mm/yr in 2017, 249 mm/yr in 2018, and 261 mm/yr in 2019. The subsidence rate increases with the flow thickness. This trend is observed for most of locations except a small area in the vicinity of the active vent where the subsidence is anomalously high. We show that the main observed trend can be well explained by a thermal compaction with a 1D mathematical model that takes into account the latent heat of crystallization, temperature dependences of physical parameters (heat capacity, thermal conductivity, density), temperature dependence of crystal concentration in the melt volume, and the percentage of uncrystallized material (glass or melt), porosity and lava layer formation rate. The much faster subsidence rates observed close to the vent can be explained by contraction of buried lava tubes that is not accounted in the thermal model.

1. Introduction

Accurate quantification of the ground movement in volcanic areas and its changes in time is very important for understanding the dynamics of volcanoes. Ground deformation is often associated with the magmatic processes at depth and its observation can, therefore, be used to constrain these processes and to explore the geometry and volume of magma plumbing systems with methods of volcanic geodesy (e.g., Fernández et al., 2017). Repetitive acquisition and differencing of digital elevation models (DEM) provides us with volumes of lava and pyroclastic deposits needed for the evaluation of the volcanic effusion rates (e.g., Poland, 2014; Dai and Howat, 2017).

Post-emplacement deformation of the lava deposits is one of the key processes affecting the evolution of the ground elevation in volcanic areas. The related subsidence may reach metric values and is observable even several years after the eruptions (e.g., Briole et al., 1997; Wittmann et al., 2017; Chen et al., 2018; Carrara et al., 2019). A spectacular example is the observation of up to 5 cm/year subsidence rate in the Parícutin lava field ~60 years after the eruption (Chaussard, 2016). This process is often described with models including the thermal cooling and compaction (Wittmann et al., 2017; Carrara et al., 2019) and the viscous relaxation of the lava substrate (Briole et al., 1997). Developing and verifying accurate approaches for predicting the lava deposits deformation is important for several reasons. First, this strong deformation can mask signals from the deep activity of the plumbing system and, therefore, should be corrected for. Second, the deposit compaction should be accounted for when estimating deposit volumes and the related effusive rates. Detailed thermal modeling and comparison of the predicted and real lava surface subsidence rates obtained from SAR interferometry allows to constrain model parameters such as mineralogical composition, temperature of phase transition, thickness, porosity, and rate of growth of lava layer. Finally, the modeling of the currently ongoing deformation can be used to estimate thicknesses and volumes of the old lava flows deposited before the satellite methods based on DEM measurements became available (Chaussard, 2016).

Many studies were devoted to modeling of the thermal cooling of a

* Corresponding author.
E-mail address: msvolkova6177@gmail.com (M.S. Volkova).

https://doi.org/10.1016/j.jvolgeores.2022.107554
Received 27 October 2021; Received in revised form 17 February 2022; Accepted 13 April 2022
Available online 19 April 2022

lava flow during volcanic eruptions of various types and to subsequent subsidence of the lava surface. Models differ in their complexity and a range of thermal parameters. Shaw et al. (1977) suggested a thermal model of the Hawaiian Alae lava lake and compared the synthetic temperature field with the measured temperature profiles obtained by drilling of the solidified lava crust by (Peck, 1978). By comparing 1D and 2D solutions Shaw et al. (1977) demonstrated that a one-dimensional model is sufficient for an adequate thermal modeling when the ratio of the thickness of the lava flow to its horizontal dimensions is small. Keszthelyi and Denlinger (1996) showed that the main mechanisms at the initial stage of lava cooling are thermal radiation, natural convection at the atmosphere – lava boundary, conductive heat transfer within the flow, dependence of thermophysical properties on temperature and porosity, as well as release of latent heat during crystallization. Neri (1998) extended this analysis considering magma as a vesiculated binary melt with a given liquidus and solidus temperature and with the possible presence of a eutectic.

Patrick et al. (2004) considered the cooling process of the lava flow formed during the 1997 eruption of Okmok volcano taking into account ambient temperature fluctuations and data on precipitation and wind strength. They argue that after lava has cooled for more than 2 years, one of the main factors controlling the heat transfer turned out to be thermal conductivity and porosity, i.e. other parameters affect the lava cooling process only at the initial stage.

Recently Chaussard (2016) presented a thermal model of the cooling lava to explain the long-term subsidence of the of Parícutin volcano lava fields (Mexico). These lavas were deposited during the eruptions of 1943–1952 and their subsidence was registered by interferometric synthetic aperture radar (hereinafter referred to as InSAR) in 2007–2011. This model takes into account radiation and convection from the lava surface, conductive heat transfer within the flow and to the ground, vesiculation and latent heat generation during magma solidification. The modeling results showed that compaction induced by cooling of a lava flow up to 200 m thick explains the real subsidence of the flow, 60 years after its formation when conductive transfer to the ground is considered.

In this paper, we study the subsidence of the basaltic lava flows deposited during the 2012–2013 eruption of the Tolbachik volcano in Kamchatka, Russia (Belousov et al., 2015; Edwards et al., 2015). This was one of the largest effusive eruptions during recent decades that emitted 0.573 km^3 of basaltic lavas forming extended flows covering ~45.8 km^2 (Gordeev and Dobretsov, 2017). This eruption was well observed with satellites resulting in accurate estimation of the thickness and area of the lava deposits (Dai and Howat, 2017; Kubanek et al., 2015; Kubanek et al., 2017). Here we perform a SAR interferometry analysis with a series of Sentinel-1 satellite images (C-band radar, European Space Agency ESA) from 2017 to 2019 to estimate the lava field surface displacement rates. These rates are then compared with the deposit thicknesses and results of thermal modeling.

Tolbachik is an active volcano in the Klyuchevskoy Volcanic Group (KVG) located in the northern termination of the Kuril Kamchatka subduction zone (inset in Fig. 1). KVG is one of the largest and most active volcanic centers in the World (e.g. Shapiro et al., 2017a) that contains 13 large strato-volcanoes three of which, Klyuchevskoy, Bezymianny and Tolbachik, have been very active in the past few decades. Accumulated scientific evidences suggest that these volcanos might be connected by a deep and extended plumbing system (e.g., Fedotov et al., 2010; Shapiro et al., 2017b; Koulakov et al., 2020; Coppola et al., 2021). The KVG eruptions are very frequent with some major events such as the Great Tolbachik Fissure Eruption (GTFE) in 1975–1976 (Fedotov, 1984) and the Tolbachik Fissure Eruption in 2012–2013, named after the 50th anniversary of the Institute of Volcanology and Seismology Far-East Branch of Russian academy of sciences (FEB RAS), TFE-50.

TFE-50 began on November 27, 2012, and lasted nearly 10 months, until September 15, 2013. Initially, on the southern slope of the Plosky

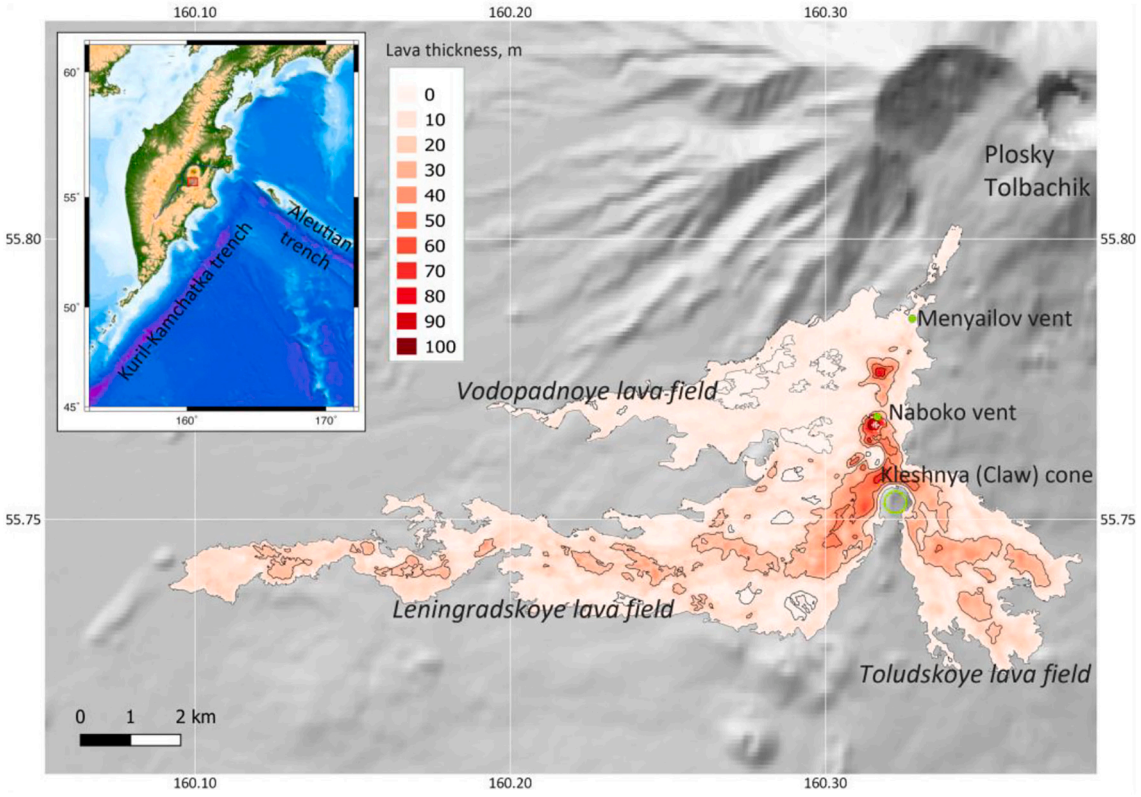

Fig. 1. Thickness of the lava flows (in meters) formed as a result of TFE-50 according to (Dai and Howat, 2017). The base map is the SRTM digital elevation model. The inset shows the location of Tolbachik in the Kamchatka Peninsula.

Tolbachik volcano, a 6 km long radial fissure was formed, oriented to the SSW. The fissure began at an altitude of about 2100 m and descended to an altitude of 1500 m. At first, lava spouting along the entire length of the fissure was observed, then after a few hours the eruption localized in two vents at altitudes of 2000 and 1600 m, named after Kamchatka volcanologists as the Menyaylov and Naboko Vents (Gordeev and Dobretsov, 2017).

The lava flow from the Menyaylov Vent divided into two main flows: the Vodopadny and Leningradsky flows (Fig. 1). Each of them was about 10 km long. The Menyaylov Vent, which was located higher, ceased its activity by December 1, 2012. Since then, the eruption occurred only from the lower Naboko Vent. By December 13, 2012, the length of the Leningradsky flow reached 16 km, and its thickness on the lateral and frontal parts was estimated as 3–15 m. When the Leningradsky flow reached the Kleshnya cone, a smaller Toludsky flow separated from it and ran south-eastward. The Toludsky flow from the Naboko Vent is 5 km long, and it stopped at an altitude of about 1100 m (Belousov et al., 2015).

The most voluminous Leningradsky lava field started to form from the first days of the eruption with an average lava flow rate of 140 m^3 /s during the first two weeks. The second important Toludsky field began to form from December 22 to 23 by a flow enveloping the lava pile that was formed upslope of the Kleshnya cone (Fig. 1). From the second half of December, the eruption was steady, with an average lava flow rate of 18–19 m^3 /s. The formation of both the Leningradsky and Toludsky fields was greatly influenced by lava channels and tubes (Dvigalo et al., 2013).

Fig. 1 shows the thickness map of the lava field constructed from data provided by Dai and Howat (2017). The authors assessed the lava thickness by differentiating two DEMs produced before and after the eruption using data from ArcticDEM, a highly accurate sub-meter resolution DEM that covers the entire Arctic region.

We use a series of Sentinel-1 SAR images from 2017 to 2019 to estimate the lava field surface displacement rates. Then, we develop a mathematical model for the magma cooling process and obtain governing parameters that provide the best consistency with data on the lava surface subsidence during its solidification. Our model takes into account the latent heat of crystallization, temperature dependences of physical parameters (heat capacity, thermal conductivity, density), temperature dependence of crystal concentration in the melt volume, and the percentage of uncrystallized material (glasses), porosity and lava layer formation rate.

2. Estimation of lava surface displacements by SAR interferometry

Measurement of the displacements of the earth's surface or man-made objects by satellite radar interferometry methods are based on the differential analysis of images taken by a synthetic aperture radar (SAR) for the same segments of the earth's surface. The radar emits an electromagnetic signal at a certain angle to the vertical, called the off-nadir angle, and receives the signal reflected from the earth's surface. The amplitude and phase of the reflected signal are recorded for each resolution element. Based on the phase shift of the signals received during the first and second surveys, we can estimate the displacements of the reflecting natural or man-made object during the time interval between two surveys (Hanssen, 2001).

Depending on the problem to be solved, researchers use methods based on analysis of a pair of images (so-called differential interferometry, DInSAR) or a series of interferograms in which so-called persistent scatterers (PS) are identified and their average displacement rates are measured using time series approaches (e.g., Ferretti et al., 2001). The former allows us to estimate surface deformations with a centimetric accuracy and the average displacement rates over the time series can be estimated at a few mm/yr.

An important indicator that controls the quality of the results obtained is the interferometric correlation of the images (coherence), which varies from 0 to 1. With low coherence (usually <0.2–0.3), it is difficult to combine (co-register) images and then assess displacements. When studying Kamchatka, we cannot always find pairs of images with a good correlation due to the peculiarities of the region, such as mountainous terrain, the presence of snow for most of the year, rapidly changing vegetation in summer, and active surface processes. Nevertheless, the SAR interferometry method has been successfully used to monitor volcanoes, including those on the Kamchatka Peninsula. Successful examples include the study of surface displacements in the Uzon caldera by (Lundgren and Lu, 2006), displacements of the slopes of Kizimen (Ji et al., 2013), Tolbachik (Lundgren et al., 2015; Kubanek et al., 2015; Kubanek et al., 2017), Karymsky (Ji et al., 2018), Bezymianny (Mania et al., 2019), Bolshaya Udina (Senyukov et al., 2020) and Koryaksky (Mikhailov et al., 2021) volcanoes.

To assess the surface displacements of the Tolbachik lava fields, we processed a time series of radar images using the Small Baseline Subset technique (SBAS, (Berardino et al., 2002)) in the SARscape software. We used 35 Sentinel-1A satellite images taken in Interferometric Wide Swath mode from the descending orbit (relative orbit number 60) during the snow-free period of 2017–2019: from May 14, 2017 to September 23, 2017 (12 images), from May 21, 2018 to September 30, 2018 (12 images) and from May 16, 2019 to September 13, 2019 (11 images).

In the SBAS technology, the available set of images is used to make all possible combinations of pairs whose spatial and temporal baselines do not exceed specified thresholds. For the Kamchatka region we set them equal to 100 m and 4–4.5 months. From the selected pairs, the stack of interferograms and their absolute phases are calculated. Once the phase values are known, the next step is to reconstruct the sequential dynamics of the displacements over time. It is followed by spatial and temporal filtering to eliminate atmospheric delay. This method is effective for natural weakly reflective terrains (Berardino et al., 2002; Lanari et al., 2004). It is also convenient because it does not impose strict requirements for the number of images in a time series, which is very important for the harsh environment of the Kamchatka region.

The SAR interferometry methods determine the displacements by the phase difference of the reflected signals, so the resulting displacements are equal to the projection of the total displacement vector in the direction along the Line Of Sight (LOS) (Hanssen, 2001). If the displacements in the horizontal directions can be considered as negligible (as is the case with cooling lava flows), with knowing the incidence angle of the satellite beam, we can calculate the displacements in the vertical direction, which we will call subvertical. According to the results of interferometric processing by the SBAS method, the maximum rates of subvertical displacements of the lava layer surface are in the region of the Kleshnya cone and have a value of 285 mm/yr for 2017, 249 mm/yr for 2018, and 261 mm/yr for 2019. The surface subsidence rates of the central and lower parts of the field do not exceed 80 mm/yr. In general, the Leningradsky field subsides slightly faster than the Toludsky field (Fig. 2).

It should be noted that interferometric processing did not allow us to obtain a continuous map of surface displacement rates for the entire region occupied by the lava flows because of the difficult terrain and loss of coherence higher up the slope. Therefore, the lava field thickness values comparable with the results obtained for the lava subsidence values from satellite data lie in the range from about 0 to 60 m. The maximum thickness of the lava field, obtained by ArcticDEM, reaches almost 100 m and is located in the vicinity of the Naboko cone (Fig. 2).

The subsidence rates for all points with measurements are compared with the lava thickness in Fig. 3a. A clear trend can be identified as dense point cloud in the upper part of this plot. Following this trend, the subsidence rate is proportional to the thickness and reaches values of ~100 mm/year for the flow thickness about 60–70 m. At the same time, a separate group of points with “anomalously” high values of the lava surface subsidence (up to 260 mm/year) can be clearly distinguished from the main “cluster”. We separate two “clusters” with drawing a limit

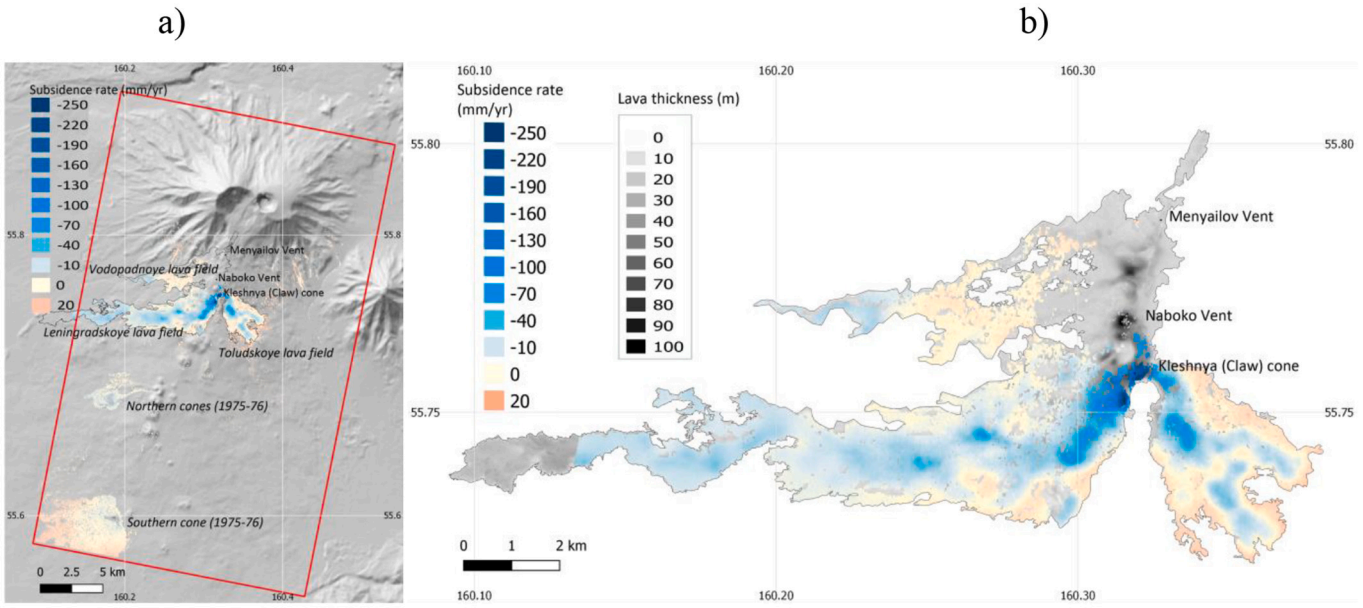

Fig. 2. (a) Map of observed lava surface displacement rates inferred from SAR interferometry and averaged between 2017 and 2019. The red rectangle outlines the study area. (b) The same map compared with the lava thickness (Dai and Howat, 2017). (For interpretation of the references to colour in this figure legend, the reader is referred to the web version of this article.)

based on a simple visual inspection (red line in Fig. 3a) and plot them with two distinct colors in a map (Fig. 3b). As a result, we see that all "anomalous" points are concentrated in a small area close to the Naboko vent and Kleshya cone while most of the surface of the lava filed subsides "normally".

At the periphery of the lava flow, especially on the Toludskoe field, SAR data shows small uplift with the rate up to 18 mm/year. Slow upward movements were also registered on the slopes of Tolbachik volcano above the TTI-50 lava fields and on the Southern cone at the southern edge of the study area (Fig. 2a). Several processes can be responsible for the regional uplift including lava migration below the Tolbachik volcano. Uplift at the border of the lava field at least partly may be a result of the horizontal heat transfer in the ground below the lava field from the central parts where temperature is high down to 50 m depth to the relatively cold ground at the periphery of the lava field (see Fig. 5c).

3. Model of the lava flow cooling

3.1. General model formulation

We consider the cooling of a lava layer, which consists of three components: liquid melt, gas, and solid crystals. Most of the gas was released during the eruption (Plechov et al., 2015), so the degassing of a stagnant lava flow can be ignored as a first order approximation. Following the detailed analysis in (Patrick et al., 2004), we can also ignore the process of convective heat and mass transfer. When the lava crust cools below the solidus temperature, we can ignore the heat radiation from its surface compared to the convective heat flux. We will consider the lava flow as an inherently homogeneous medium consisting of a magmatic melt and some initial volume of crystals. Strictly speaking, weight of the loading mass also leads to compaction and subsidence. But seven years after lava emplacement this process can be ignored.

Horizontal dimensions of the flow are significantly larger than the vertical, and a small parameter equal to the ratio of the lava flow thickness to its length can be introduced. Dimensionless analysis shows that the temperature derivatives along the horizontal coordinates are much smaller compared to the vertical one. Therefore, the horizontal temperature changes can be ignored, and we can solve the one-dimensional problem along the vertical coordinate z. Many studies of stagnant lava flow cooling have also used the 1D formulations (Neri, 1998; Shaw et al., 1977; Patrick et al., 2004; Chaussard, 2016).

According to the physical properties, the modelled medium is divided into a lava layer and an underlying rock layer. To discretize the modeling domain, we introduce a grid of elements with a step $\Delta z_i(t)$, $i = 1, \ldots, N$; where N is the number of grid elements that determines the size of the model. The Oz axis is directed downward, and the origin of coordinates is aligned with the bottom of the lava layer.

As the phase change (formation of crystals from the melt) is accompanied by the latent heat release during lava cooling, the problem results in solving a 1D energy equation with advection due to subsidence and volumetric heat source:

$$\frac{\partial T}{\partial t} = \frac{\partial}{\partial z}\left(k\frac{\partial T}{\partial z}\right) + W(z,t)\frac{\partial T}{\partial z} + Q(z,t,T) \quad (1)$$

with initial and boundary conditions:

$$T(z, t=0) = \begin{cases} T_{melt}; for\ z \in [-H_{ini}; 0]; \\ dT_0{}^*z; for\ z \in (0; H_{max}]; \end{cases} \quad (2)$$

$$T(-H_{ini}, t) = 0; T(H_{max}, t) = dT_0{}^*H_{max},$$

where $T(z,t)$ and $W(z,t)$ are the temperature and subsidence rate of the lava at the depth z at time t; $Q(z,t,T) = L/c_p * \partial X_{faz}(z,T)/\partial t$ is the amount of the latent heat released per unit volume during the phase change (crystallization); $X_{faz}(z,T)$ is the proportion of the solid phase at the depth z. L is the latent heat of crystallization, c_p is the specific heat capacity, and $k(t,z)$ is the thermal diffusivity. The initial thickness of the lava layer is equal to H_{ini}. The depth of the model's lower boundary, H_{max}, is set big enough to assume that temperature changes below this boundary can be ignored, T_{melt} is the initial temperature of the melt, dT_0 is the temperature gradient in the soil by the time the eruption begins.

Lava density depends on its composition, temperature, presence of pores, and the amount of crystallized (crystals) and uncrystallised (glass/melt) components. Let us introduce the fraction of solidified part of the lava $X(t,T)$, equal to the equilibrium fraction of crystals calculated for crystallization of the most primitive TFE-50 lava in the Petrolog 3 software (Danyushevsky, Danyushevsky and Plechov, 2011). Let X_{cr}, X_{gl}

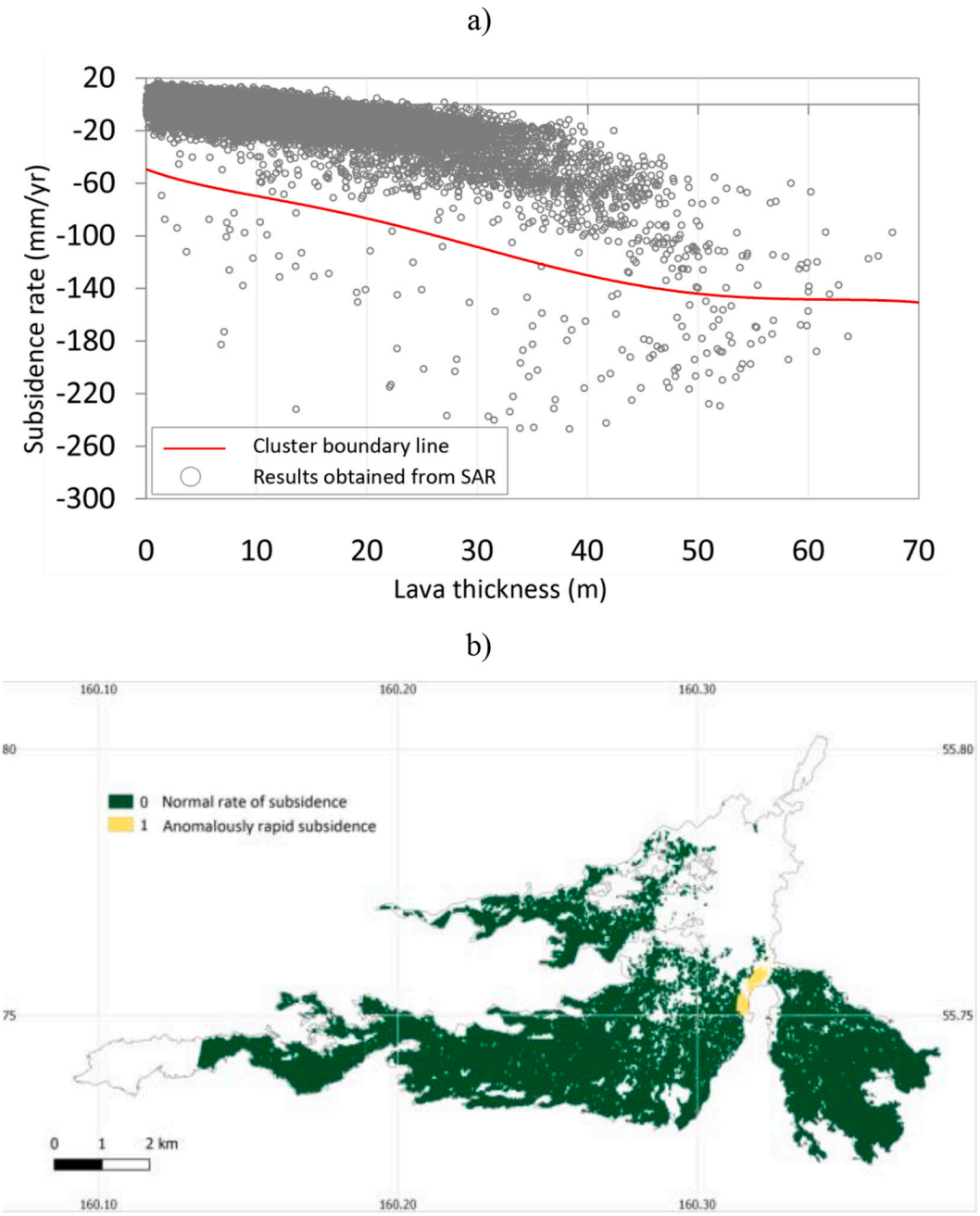

Fig. 3. (a) Comparison of subsidence rates measured from SAR data with the lava thickness. Red line defines the boundary between the "normal" and "anomalous" clusters. (b) Geographical locations of points with normal (green) and anomalous (yellow) subsidence rates. (For interpretation of the references to colour in this figure legend, the reader is referred to the web version of this article.)

and X_{por} be the volume fractions of crystals, glass and pores (gas) in the solidified part of the lava, which we will consider independent of time and temperature: $X_{cr} + X_{gl} + X_{por} = 1$. The molten part consists of magmatic melt and gas in the pores, with the porosity of the melt being also equal to X_{por}. These are average values for the flow thickness, although in the upper part (crust) and the massive main part the fractions of pores and crystals will be different.

We will consider X_{gl} and X_{por} to be free parameters, and adjust their values by comparison with the data on the lava surface subsidence. We used the following parameters as the initial ones:

$X_{gl} = 0.2$, $X_{por} = 0.1$, then $X_{cr} = 1 - (X_{gl} + X_{por}) = 0.7$.

The density of molten part of lava (ρ_{lava}) is:

$$\rho_{lava}(t, T_{melt}) = \rho_{melt} * (1 - X_{por}) + \rho_{por}(t, T) * X_{por},$$

where ρ_{melt} is the density of the melt, ρ_{por} is the density of the gas filling the pores.

The solidified part consists of crystals with the density $\rho_{cr}(t, T)$, glass with the density $\rho_{gl}(t, T)$ and gas in the pores ($\rho_{por}(t, T)$). Then the density of the solidified part - ρ_{solid}, is:

$$\rho_{solid}(t, T) = \rho_{cr}(t, T) * X_{cr} + \rho_{gl}(t, T) * X_{gl} + \rho_{por}(t, T) * X_{por},$$

and the density of the lava containing the melt and the solidified part (both with the gas fraction X_{por}) is:

$$\rho_{total}(t,T) = \rho_{solid}(t,T)*X(t,T) + \rho_{lava}(t,T)*(1 - X(t,T)).$$

By substituting the densities of the lava and the solidified part here, one will get:

$$\rho_{total}(t,T) = \left(\rho_{cr}(t,T)*X_{cr} + \rho_{gl}(t,T)*X_{gl} + \rho_{por}(t,T)*X_{por}\right)*X(t,T) + \left(\rho_{melt}*\left(1 - X_{por}\right) + \rho_{por}(t,T)*X_{por}\right)*(1 - X(t,T)),$$

or after reducing the terms with $\rho_{por}(t,T)$:

$$\rho_{total}(t,T) = \left(\rho_{cr}(t,T)*X_{cr} + \rho_{gl}(t,T)*X_{gl}\right)*X(t,T) + \rho_{melt}*\left(1 - X_{por}\right)*(1 - X(t,T)) + \rho_{por}(t,T)*X_{por}, \quad (3)$$

Now in Eq. (1), the heat released during crystallization will be:

$$Q(z,t,T) = L/c_p*\partial X_{faz}(z,T)/\partial t = L/c_p*X_{cr}*\partial X(z,T)/\partial t$$

because some part of the melt transforms into glass during solidification and the energy released during this process can be ignored.

In the modeling, the density of crystals $\rho_{cr}(t,T)$ is calculated from the equilibrium density of crystal assemblage (Pl, Ol, Cpx) with account of their compositions (An, Fo and Mg#). These properties were calculated in Petrolog 3 software (Fig. 4).

The glass density is close to the melt density and changes only due to cooling:

$$\rho_{gl}(t,T) = \rho_{melt}*\left(1 - \alpha_{v\_glass}*\left(T - T^{(0)}_{melt}\right)\right),$$

where α_{v_glass} stands for the coefficient of thermal expansion of glass equal to $5.8*10^{-7}$ 1/degC, the melt density is assumed constant ρ_{melt}=2.6428 g/cm^3 and corresponds to the density at $T^{(0)}_{melt}$=1100 °C (Fig. 4A), the gas density in the pores $\rho_{por}(t,T)$ can also be assumed constant 0.001 g/cm^3, since its contribution is negligibly small.

The height of all grid elements Δz_i is recalculated at each time step due to temperature changes. That allows calculation of the displacement rate $W(z,t)$ in Eq. (1) using conservation of mass $\rho(t,T)$ * $\Delta z(t,T)$ = $\rho(T_{melt})$ * $\Delta z(T_{melt})$. Thus:

$$\Delta z(t,T) = \Delta z(T_{melt})*\rho(T_{melt})/\rho(t,T). \quad (4)$$

The crystal density and thermal expansion coefficient α_v depend on the crystal composition. We use a value averaged over the minerals that make up the Tolbachik lava. Below the solidus, the density is calculated as a function of temperature:

$$\rho_{cr}(t,T) = \rho^{(0)}\left(1 - \alpha_v\left(T(t) - T^{(0)}_{cr}\right)\right), \quad (5)$$

with parameters $T^{(0)}_{cr}$ = 505 °C; $\rho^{(0)}$ is equal to the equilibrium density value of 2.9752 g/sm^3 at the temperature $T^{(0)}_{cr}$. Eq. (5) corresponds to the slope of the curve in Fig. 4A.

Porosity decreases from 54 vol% to 6 vol% during the flow of lava. Then, during solidification, presumably due to additional volatile release, the porosity slightly increased again to 8 vol% (Plechov et al., 2015). In the upper parts of the flow, the porosity is relatively high (35 vol%). Individual samples of aa-lava picked up at the surface of the lava flow are similar to solidified foam, with an assessed porosity up to 75% (Gordeev and Dobretsov, 2017).

The model also accounts for the incremental formation of the lava flow. It is assumed that the lava layer with the thickness $H(t)$ is formed during the first year (the year of the eruption) at the constant rate dh/dt, where dh is the given increment in meters over the time dt, so that $H(t) = t \times dh/dt$. In the first year, a layer of cells with the given thickness dh was added to the model at the top of the flow at the equal time intervals dt

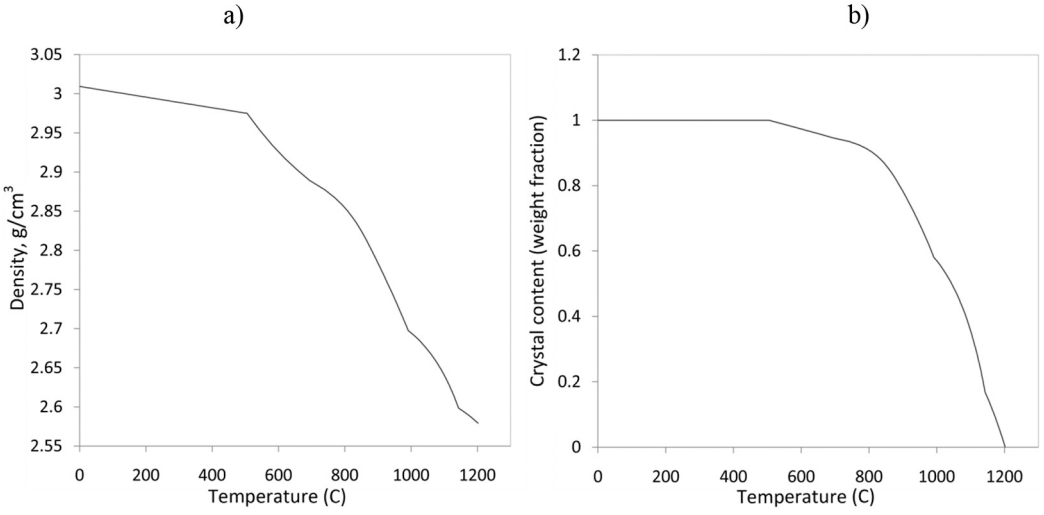

Fig. 4. Temperature dependencies of magma density (g/cm^3) (a) and crystal content (weight fraction) in the melt (b), as determined from laboratory data using the Petrolog 3 software (Danyushevsky, Danyushevsky and Plechov, 2011).

until the given final thickness of the lava layer H_{fin} was reached. It was assumed that at the time t_0 the thickness of the flow is equal to H_{ini}.

3.2. Model parameters

Eqs. (1)–(2) are solved in the domain with dimensions: $H(t) + H_{max}$, where $H(t)$ is the thickness of the lava layer for different scenarios of its build-up dh/dt (the final thickness value H_{fin} varied from 10 to 60 m), H_{max} is the thickness of the soil layer. The grid step along z in the lava layer is 0.1 m, the grid step along z in the soil layer (i.e. from $z = 0$ to $z = H_{max}$) increases with depth, the time step is $\tau = 0.5$ of a day.

The initial temperature of the melt is $T_{melt} = 1100$ °C, the initial temperature gradient with depth in the underlying rocks before the eruption is assumed as $dT_0 = 50$ °C/km; the specific heat of crystallization $L = 3.5*10^5$ J/kg; the thermal expansion coefficient α_v of igneous material corresponds to the density model in Fig. 4a.

The heat capacity c_p and thermal conductivity λ are given the following temperature dependences: for c_p (J/kg/K) according to (Patrick et al., 2004):

$$c_p(T) = 1100 \text{ for } T > 1010 \text{ K};$$

$$c_p(T) = 1211 - \left(1.12*10^5\right)/\text{T for } T < 1010 \text{ K};$$

for λ (W/m/K) according to (Hidaka et al., 2005):

$$\lambda(T) = 1.15 + 5.9*10^{-7}*(T - 1200C)^2, \text{for T} < 1200^{o}\text{C}$$

$$\lambda(T) = 1.15 + 9.7*10^{-6}*(T - 1200C)^2, \text{for T} > 1200^{o}\text{C}$$

The porosity and percentage content of glass were considered free

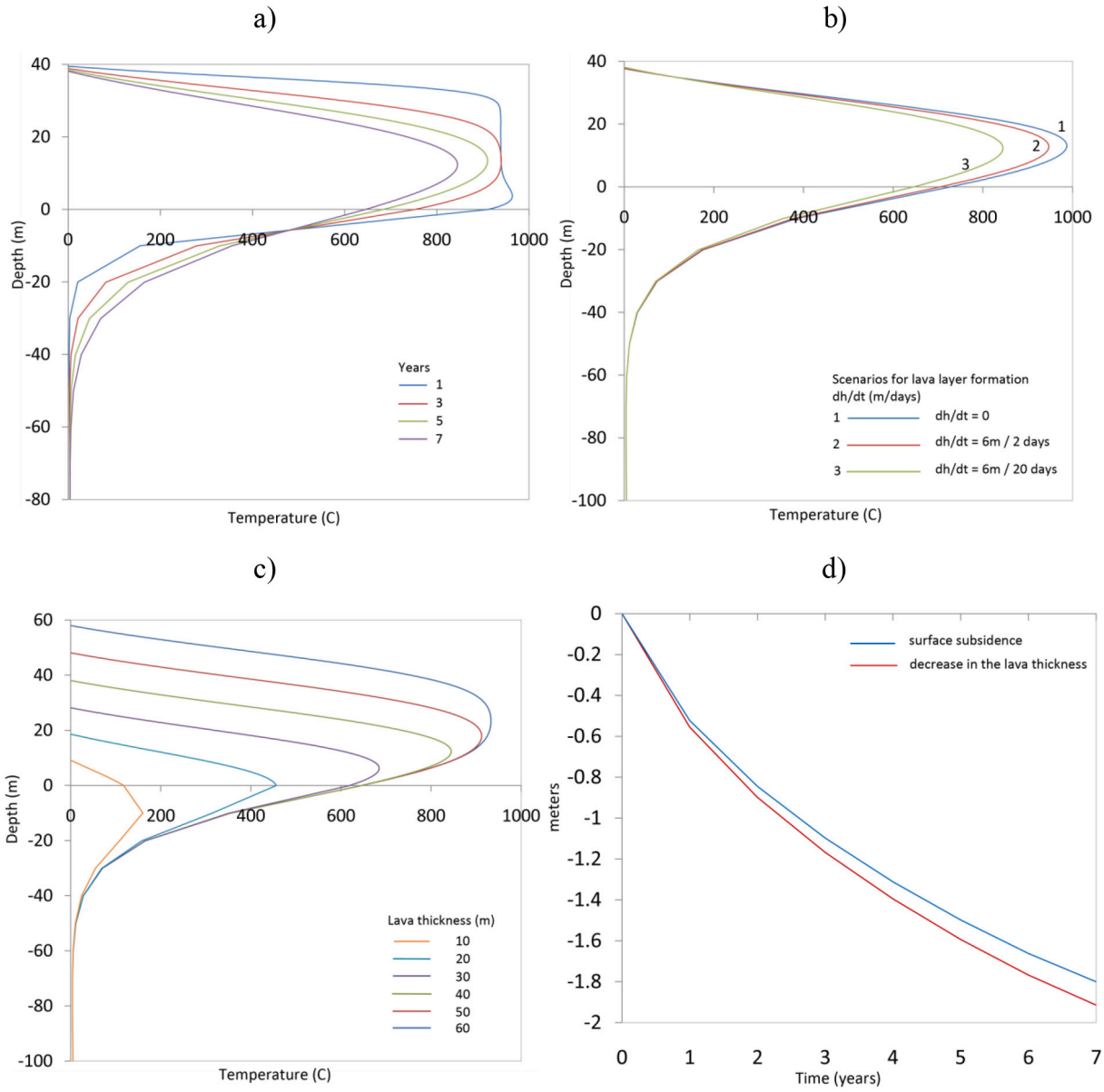

Fig. 5. (a) Temperature profiles 1, 3, 5, and 7 years after the eruption with a slow layer build-up (dh/dt = 6 m per 20 days) and $H_{fin} = 40$ m. (b) Temperature profiles 7 years after the eruption for $H_{fin} = 40$ m for different scenarios: 1 – instantaneous layer formation (dh/dt = 0); 2 and 3 – fast (dh/dt = 6 m per 2 days) and slow (dh/dt = 6 m per 20 days) growing layers, respectively. (c) Temperature profiles 7 years after the eruption for different lava flow thicknesses: H_{fin} from 10 to 60 m (dh/dt = 6 m per 20 days). (d) Time evolution of the lava thickness and surface subsidence (red and blue colors, respectively) for a layer with: $H_{fin} = 40$ m, dh/dt = 6 m per 20 days. A porosity of 10% and a glass content of 20% have been used in all shown simulations. (For interpretation of the references to colour in this figure legend, the reader is referred to the web version of this article.)

parameters and selected by comparing the calculated and actual data on the lava flow surface subsidence.

Given the year of the eruption, the modeling period t was 7 years (2012–2019). The dynamics of lava flow formation and cooling involves different physical and geological processes. In our model, we focused on the thermal subsidence that plays a dominant effect in the evolution of the lava flow thickness.

3.3. Accounting for the lava thickness build-up rate

We considered several scenarios for the lava layer formation for numerical modeling. Because the eruption lasted 10 months, and the maximum thickness of the accumulated lava (Dai and Howat, 2017) reached 100 m (the Naboko cone region), the vertical rate of layer increment dh/dt must meet these time constraints. In general, the lower the rate of layer build-up dh/dt results in faster cooling and slower lava subsidence during the 7th year after the eruption. If the layer builds up quickly, it cools down more slowly, resulting in a greater lava subsidence during the 7th year. For the model with a growing layer, we chose two extreme scenarios: "fast" and "slow". The increment thickness of the lava flow was set constant and equal to 6 m; the same thickness was set to the initial layer H_{ini}. In case of the fast formation, the lava layer grew at a rate of 6 m in 2 days, and in case of the slow formation 6 m in 20 days. These values provide time intervals of lava accumulation that do not extend beyond the eruption timeline. The modeling was also performed without accounting for the layer build-up, where the lava layer at time $t = 0$ already had the given thickness H_{fin}.

4. Relationship between the thermal cooling and surface subsidence

Fig. 5 shows temperature profiles computed assuming 10% porosity and 20% of glass and different rates of lava flow emplacement. Because most of the lava field has thicknesses between 20 and 40 m, we mainly consider a 40 m thick layer. Fig. 5a shows how the temperature evolves during 7 years within a 40 m thick layer formed with $dh/dt = 6$ m per 20 days. It shows a progressive cooling of the lava layer and heating of the underlying crust. For such "slow" scenario, the temperature at the base of the lava flow by the end of the first year is higher due to the addition of new overlying layers of molten magma in the first year. Over time, lava cools down and after 7 years its maximum temperature is ~845 °C, with an equilibrium crystallinity of about 86.7%, implying that the crystallization process is not yet completed. Fig. 5b shows that with the slow lava emplacement, the temperature in the middle of the layer by the end of the 7th year is almost 150 °C lower than with the fast and instantaneous emplacement. Fig. 5c shows that the maximum temperature in the layer depends strongly on its thickness. For a 60 m layer, by the end of the 7th year, there is still a melt in the middle of the flow. In a 30 m layer, the crystallization process in the middle of the layer is already completed after 7 years. Layers with a thickness smaller than 40 m reach crystallinity >54% by the end of the 7th year after the eruption and their subsidence slows down considerably. At the same time, lavas with a thickness of above 50 m after 7 years still contain melt layers. Time evolution of the surface displacement and the lava thickness in a 40 m lava layer are shown in Fig. 5d. Note, that the layer thinning is slightly faster than the surface subsidence because of the small contribution of the heating of the underlying crust.

5. Comparison of the modeling with the results of SAR interferometry

Fig. 6 shows the comparison of the observations with the modeling results assuming different percentages of pores and glasses in the igneous material of slow flow formation at $dh/dt = 6$ m per 20 days. We use this comparison to assess the effect of porosity and glass content in the lava on its subsidence. Calculations in Fig. 6 show that an increase in

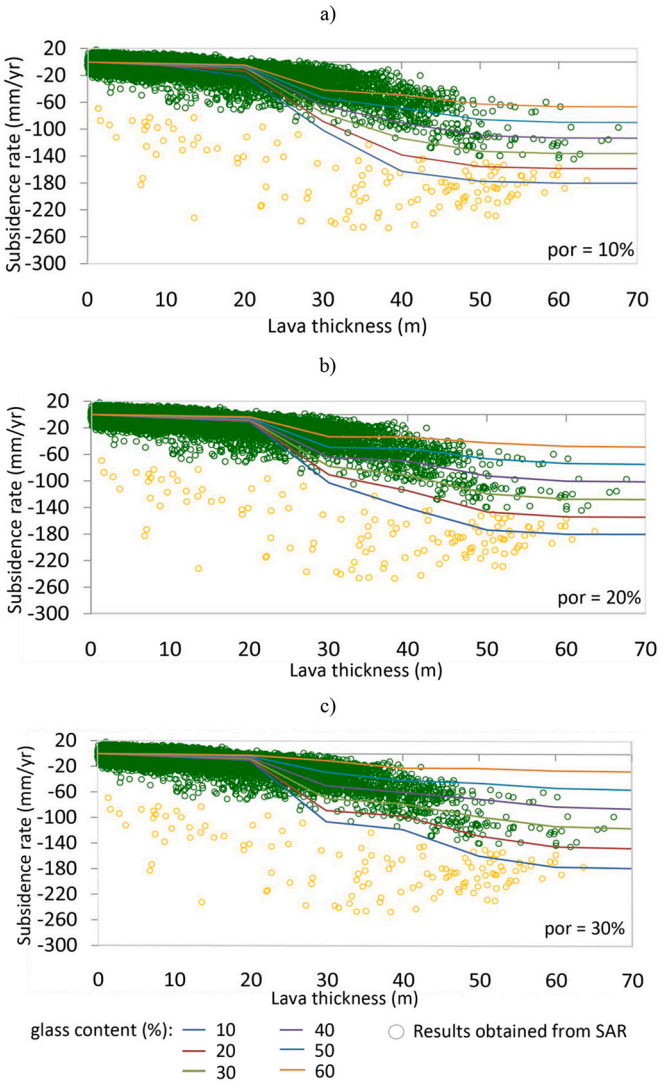

Fig. 6. Assessment of the effect of porosity and glass content in the lava on the subsidence rate. The colored curves show results of the modeling with different glass content for three different values of porosity: (a) 10%, (b) 20%, (c) 30%.

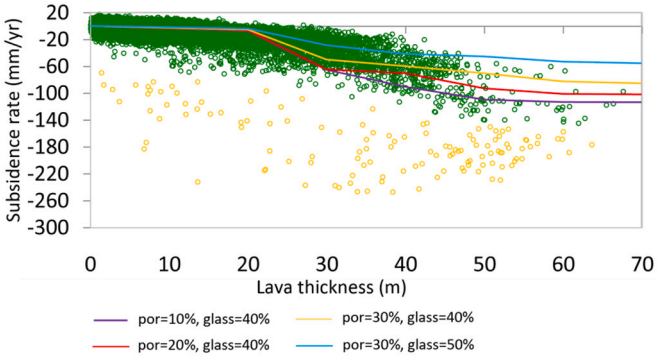

Fig. 7. Results of the modeling with parameters best fitting the "normal" trend of the lava surface subsidence (green circles). Yellow circles are values from the "anomalous" zone of subsidence. "Slow layer build-up" scenario (dh/dt = 6 m/20d) has been considered. (For interpretation of the references to colour in this figure legend, the reader is referred to the web version of this article.)

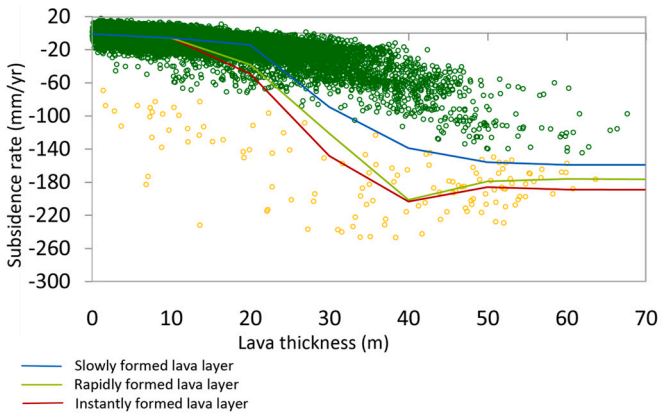

Fig. 8. Comparison of results obtained from SAR interferometry data (green circles - "normal" rate, yellow circles - "anomalous" rate) with modeling results (colored lines) at 10% porosity and 20% glass content, which better fit to "anomalous" subsidence. The vertical axis is the surface subsidence rate in 2019 (in mm/yr). The red line is the result for an instantaneous layer formation ($H_{ini} = H_{fin}$, dh/dt = 0). The green line is the rapidly formed lava layer (dh/dt = 6 m during 2 days). The blue line is the slowly formed lava layer (dh/dt = 6 m during 20 day). (For interpretation of the references to colour in this figure legend, the reader is referred to the web version of this article.)

the glass quantity in the final lava composition, similarly to an increase in porosity, leads to a decrease in the lava surface subsidence rate during the 7th year.

Fig. 7 shows the results of modeling with parameters that fit well the "normal" trend of lava subsidence (green circles). These curves have been obtained with considering a "slow layer build-up" scenario (*dh/dt* 6 m during 20 days).

We also performed simulations with other possible rates of the lava thickness build-up. Fig. 8 shows the results of such modeling with 10% porosity and 20% glass content compared with the observations. Scenarios of rapidly (*dh/dt* 6 m during 2 days) or instantly formed lava layer fit better the observations in the "anomalous" zone (yellow circles).

6. Discussion and conclusions

Our observations of surface subsidence of the lava flows emitted by the 2012–2013 Tolbachik eruption based on SAR interferometry show two distinct trends. In more than 90% of locations, the subsidence vs. lava thickness follows the main "normal" trend that can be well explained by a model based on thermal cooling and compaction of deposited lavas. So far, the subsidence rate observed in the majority of the Tolbachik lava field can be directly compared with those reported by Wittmann et al. (2017) who observed a ~ 20 mm/year vertical velocity for ~5 years old and ~ 20 m thick lava flows in Hekla, Iceland. This subsidence rate is very close to our observations for the "normal" part of the Tolbachik fields (Fig. 3a). The considered simple model allows us to fit this main trend inferred from the satellite-based measurements of the lava subsidence rates with varying just a few free parameters. The best fit to SAR data was achieved for the slowly formed lava layer (*dh/dt* = 6 m during 20 day) with porosity being between 10 and 30% and glass content between 30 and 50%.

At the same time, a relatively small number of points clearly show much faster subsidence in comparison with this "normal" trend. All these "anomalous" points are located in a small compact area in the vicinity of the Naboko vent and Kleshnya cone. The emergence of this region with high lava surface subsidence rates can be explained by the specific conditions of lava flow formation.

One possibility is that this part of the flow was formed very quickly after the active vent opening, which is different from more distant parts of the lava fields growing more progressively. Indeed, computations based on scenarios of "fast" or "instant" lava layer formation predict significantly faster subsidence rates for layers thicker than 25 m (Fig. 8).

At the same time, a considerable number of "anomalous" points are observed in the relatively thin part of the flow and cannot be solely explained by the model based on thermal compaction. Therefore, other processes should be considered for explaining the full range of observations. During the eruption, a system of lava tubes and channels was formed in the upper part of the flow just beneath the Naboko vent. These tubes were emptied during the eruption with lava flowing to the outer part of the field resulting in formation of many cavities. The region of the anomalously fast subsidence likely corresponds to a collapse of such "lava caves". So far, episodes of such very fast subsidence have been observed during the eruption. For example, the lava surface elevation seen from the sky window southward from the Naboko cone dropped by ~5 m between February and May 2013 (Gordeev and Dobretsov, 2017). Six-seven years after the eruption, a significant number of large cavities are still present under the solidified top of the basaltic flow in the region where the satellite data measure high subsidence rates.

Overall, our results for the well-documented Tobachik eruption show that while most of the measured lava subsidence can be well explained by a simple thermal compaction model, the largest observed values can be at least in part due to other processes such as collapsing cavities within the lava deposits. Therefore, the possibility of such mechanisms should be systematically considered when interpreting the observations in other regions.

Funding

This work was supported by grant N⁰14.W03.31.0033 of the Ministry of Education and Science "Geophysical research, monitoring and forecasting of catastrophic geodynamic processes in the Russian Far East" and by the European Research Council under the European Union Horizon 2020 research and innovation program (Grant Agreement 787399-SEISMAZE).

Author statement

M.S. Volkova: SAR data processing, state of problem, numerical solution, interpretation, writing and editing. N.M. Shapiro, O.E. Melnik, V. O. Mikhailov: problem formulation, methodology, interpretation, writing and editing. P. Yu. Plechov: mineral composition and thermophysical properties of the Tolbachik lavas. O.V. Bergal-Kuvikas: modeling of temperature dependencies using the Petrolog 3 software. E.P. Timoshkina: methodology, numerical solution, interpretation.

Declaration of Competing Interest

The authors declare that they have no known competing financial interests or personal relationships that could have appeared to influence the work reported in this paper.

Acknowledgments

We thank Chunli Dai and Ian Howat for providing lava field thickness data constructed from the optical survey data. We also thank the European Space Agency for providing Sentinel-1A images. We thank both anonymous reviewers for suggestions and corrections which helped to improve the manuscript.

References

Belousov, A., Belousova, M., Edwards, B., Volynets, A., Melnikov, D., 2015. Overview of the precursors and dynamics of the 2012–13 basaltic fissure eruption of Tolbachik Volcano, Kamchatka, Russia. J. Volcanol. Geotherm. Res. 307 (2015), 22–37. https://doi.org/10.1016/j.jvolgeores.2015.04.009.

Berardino, P., Fornaro, G., Lanari, R., Sansosti, E., 2002. A new algorithm for surface deformation monitoring based on Small Baseline Differential SAR Interferograms. IEEE Trans. Geosci. Remote Sens. 40 (11), 2375–2383.

Briole, P., Massonnet, D., Delacourt, C., 1997. Post-eruptive deformation associated with the 1986–87 and 1989 lava flows of Etna detected by radar interferometry. Geophys. Res. Lett. 24 (1), 37–40. https://doi.org/10.1029/96GL03705.

Carrara, A., Pinel, V., Bascou, P., Chaljub, E., De la Cruz-Reyna, S., 2019. Post-emplacement dynamics of andesitic lava flows at Volcán de Colima, Mexico, revealed by radar and optical remote sensing data. J. Volcanol. Geotherm. Res. 381, 1–15. https://doi.org/10.1016/j.jvolgeores.2019.05.019.

Chaussard, E., 2016. Subsidence in the Parícutin lava field: Causes and implications for interpretation of deformation fields at volcanoes. J. Volcanol. Geotherm. Res. 320, 1–11. https://doi.org/10.1016/j.jvolgeores.2016.04.009.

Chen, Y., Zhang, K., Froger, J.-L., Tan, K., Remy, D., Darrozes, J., Peltier, A., Feng, X., Li, H., Villeneuve, N., 2018. Long-term subsidence in lava fields at Piton de la Fournaise Volcano measured by InSAR: new insights for interpretation of the eastern flank motion. Remote Sens. 10 (4), 597. https://doi.org/10.3390/rs10040597.

Coppola, D., Marco, L., Massimetti, F., Hainzk, S., Schevchenko, A.V., Mania, R., Shapiro, N.M., Walter, T.R., 2021. Thermal remote sensing reveals communication between volcanoes of the Klyuchevskoy Volcanic Group. Sci. Rep. 11, 13090. https://doi.org/10.1038/s41598-021-92542-z.

Dai, C., Howat, I.M., 2017. Measuring lava flows with ArcticDEM: Application to the 2012–2013 eruption of Tolbachik, Kamchatka. Geophys. Res. Lett. 44 (12) https://doi.org/10.1002/2017GL075920, 133–12,140.

Danyushevsky, L.V., Plechov, P., 2011. Petrolog3: Integrated software for modeling crystallization processes. Geochem. Geophys. Geosyst. 12 (7) https://doi.org/10.1029/2011GC003516. Jul.

Dvigalo, V.N., Yu Svirid, I., Shevchenko, A.V., 2013. The first quantitative estimates of parameters for the Tolbachik Fissure Eruption of 2012–2013 from aerophotogrammetric observations. J. Volcanol. Seismol. 8 (5), 261–268.

Edwards, B.R., Belousov, A., Belousova, M., Volynets, A., 2015. Introduction to the 2012–2013 Tolbachik eruption special issue. J. Volcanol. Geotherm. Res. 307, 1–2. https://doi.org/10.1016/j.jvolgeores.2015.12.001.

Fedotov, S.A. (Ed.), 1984. Great Fissure Tolbachik Eruption. Kamchatka. 1975–1976. Moscow, Nuaka, p. 637.

Fedotov, S., Zharinov, N., Gontovaya, L., 2010. The magmatic system of the Klyuchevskaya group of volcanoes inferred from data on its eruptions, earthquakes, deformation, and deep structure. J. Volcanol. Seismol. 4 (1), 1–33. https://doi.org/10.1134/S074204631001001X.

Fernández, J., Pepe, A., Poland, M.P., Sigmundsson, F., 2017. Volcano geodesy: recent developments and future challenges. J. Volcanol. Geotherm. Res. 344, 1–12. https://doi.org/10.1016/j.jvolgeores.2017.08.006.

Ferretti, A., Prati, C., Rocca, F., 2001. Permanent scatterers in SAR interferometry. IEEE Trans. Geosci. Remote Sens. 39 (1), 8–20.

Gordeev, E.I., Dobretsov, N.L., 2017. 2012–2013 Tolbachik Fissure Eruption (TFE-50). SB RAS, Novosibirsk, Izd, p. 427.

Hanssen, R.F., 2001. Radar Interferometry: Data Interpretation and Error Analysis. Kluwer Academic Publishers, Dordrecht, p. 308.

Hidaka, M., Goto, A., Umino, S., Fujita, E., 2005. VTFS project: Development of the lava flow simulation code LavaSIM with a model for three-dimensional convection, spreading, and solidification. Geochem. Geophys. Geosyst. 6 (7).

Ji, L., Lu, Z., Dzurisin, D., Senyukov, S., 2013. Pre-eruption deformation caused by dike intrusion beneath Kizimen volcano, Kamchatka, Russia, observed by InSAR. J. Volcanol. Geotherm. Res. 256, 87–95.

Ji, L., Izbekov, P., Senyukov, S., Lu, Z., 2018. Deformation patterns, magma supply, and magma storage at Karymsky Volcanic Center, Kamchatka, Russia, 2000–2010, revealed by InSAR. J. Volcanol. Geotherm. Res. 352, 106–116.

Keszthelyi, L., Denlinger, R., 1996. The initial cooling of pahoehoe flow lobes. Bull. Volcanol. 58, 5–18.

Koulakov, I., Shapiro, N.M., Sens-Schönfelder, C., Luehr, B.G., Gordeev, E.I., Jakovlev, A., Abkadyrov, I., Chebrov, D.V., Bushenkova, N., Droznina, S.Y., Senyukov, S.L., Novgorodova, A., Stupina, T., 2020. Mantle and crustal sources of magmatic activity of Klyuchevskoy and surrounding volcanoes in Kamchatka inferred from earthquake tomography. J. Geophys. Res. Solid Earth 125, e2020JB020097. https://doi.org/10.1029/2020JB020097.

Kubanek, Julia, et al., 2015. Lava flow mapping and volume calculations for the 2012–2013 Tolbachik, Kamchatka, fissure eruption using bistatic TanDEM-X InSAR. Bull. Volcanol. 77 (12), 1–13.

Kubanek, Julia, Westerhaus, Malte, Heck, Bernhard, 2017. TanDEM-X time series analysis reveals lava flow volume and effusion rates of the 2012–2013 Tolbachik, Kamchatka fissure eruption. J. Geophys. Res. Solid Earth 122 (10), 7754–7774.

Lanari, R., Mora, O., Manunta, M., Mallorqui, J.J., Berardino, P., Sansosti, E., 2004. A small-baseline approach for investigating deformations on full-resolution differential SAR interferograms. IEEE Trans. Geosci. Remote Sens. 42 (7), 1377–1386. https://doi.org/10.1109/TGRS.2004.828196.

Lundgren, P., Lu, Z., 2006. Inflation model of Uzon caldera, Kamchatka, constrained by satellite radar interferometry observations. Geophys. Res. Lett. 33 (6).

Lundgren, P., Kiryukhin, A., Milillo, P., Samsonov, S., 2015. Dike model for the 2012–2013 Tolbachik eruption constrained by satellite radar interferometry observations. J. Volcanol. Geotherm. Res. https://doi.org/10.1016/j.jvolgeores.2015.05.011.

Mania, R., Walter, T.R., Belousova, M., Belousov, A., Senyukov, S.L., 2019. Deformations and morphology changes associated with the 2016–2017 eruption sequence at Bezymianny Volcano, Kamchatka. Remote Sens. 11 (11), 1278.

Mikhailov, V.O., Volkova, M.S., Timoshkina, E.P., Shapiro, N.M., Smirnov, V.B., 2021. On the connection between the koryaksky volcano activation in 2008-2009 and the underlying magmatic processes. Fiz. Zemli. 57 (6), 819–824. https://doi.org/10.1134/S1069351321060045.

Neri, A., 1998. A local heat transfer analysis of lava cooling in the atmosphere: application to thermal diffusion-dominated lava flows. J. Volcanol. Geotherm. Res. 81, 215–243.

Patrick, M.R., Dehn, J., Dean, K., 2004. Numerical modeling of lava flow cooling applied to the 1997 Okmok eruption: Approach and analysis. J. Geophys. Res. Solid Earth 109 (B3).

Peck, D.L., 1978. Cooling and vesiculation of Alae lava lake, Hawaii. In: Tech. Rep., U. S. Govt. Print. Off.

Plechov, P., Blundy, J., Nekrylov, N., Melekhova, E., Shcherbakov, V., Tikhonova, M.S., 2015. Petrology and volatile content of magmas erupted from Tolbachik Volcano, Kamchatka, 2012–13. J. Volcanol. Geotherm. Res. 307, 182–199.

Poland, M.P., 2014. Time-averaged discharge rate of subaerial lava at Kīlauea Volcano, Hawai'i, measured from TanDEM-X interferometry: Implications for magma supply and storage during 2011–2013. J. Geophys. Res. Solid Earth 119, 5464–5481. https://doi.org/10.1002/2014JB011132.

Senyukov, S.L., Mikhailov, V.O., Nuzhdina, I.N., Kiseleva, E.A., Droznina, S.Ya., Timofeeva, V.A., Volkova, M.S., Shapiro, N.M., Kozhevnikova, T.Yu., Nazarova, Z.A., Sobolevskaya, O.V., 2020. Simultaneous Study of Seismicity and Sentinel-1A Data to Assess the possible Eruption of the Extinct Bolshaya Udina Volcano. Volcanol. Seismol. 5, 26–39. https://doi.org/10.31857/S0203030620050053.

Shapiro, N.M., Sens-Schönfelder, C., Lühr, B.G., Weber, M., Abkadyrov, I., Gordeev, E.I., Koulakov, I., Jakovlev, A., Kugaenko, Y.A., Saltykov, V.A., 2017a. Understanding Kamchatka's extraordinary volcano cluster. Eos 98 (7), 12–17. https://doi.org/10.1029/2017EO071351.

Shapiro, N.M., Droznin, D.V., Droznina, S.Y., Senyukov, S.L., Gusev, A.A., Gordeev, E.I., 2017b. Deep and shallow long-period volcanic seismicity linked by fluid-pressure transfer. Nat. Geosci. 10 (6), 442–445. https://doi.org/10.1038/ngeo2952.

Shaw, H.R., Hamilton, M.S., Peck, D.L., 1977. Numerical analysis of lava lake cooling models: part I, description of the method. Am. J. Sci. 277, 384–414.

Wittmann, W., Sigmundsson, F., Dumont, S., Lavallée, Y., 2017. Post-emplacement cooling and contraction of lava flows: InSAR observations and a thermal model for lava fields at Hekla volcano, Iceland. J. Geophys. Res. Solid Earth 122, 946–965. https://doi.org/10.1002/2016JB013444.